Block Copolymer Lithography of Rhodium Nanoparticles for High Temperature Electrocatalysis
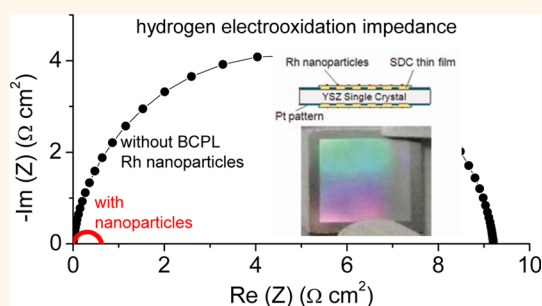
David A. Boyd,[†,*] Yong Hao,[‡,⊥] Changyi Li,[§,∥] David G. Goodwin,[‡] and Sossina M. Haile[§,‡,*]

[†]Division of Physics, Mathematics & Astronomy, California Institute of Technology, Pasadena, California 91125, United States, [‡]Division of Engineering and Applied Science, California Institute of Technology, Pasadena, California 91125, United States, and [§]Division of Chemistry and Chemical Engineering, California Institute of Technology, Pasadena, California 91125, United States. [⊥]Present address: Institute of Engineering Thermophysics, Chinese Academy of Sciences, 11 Beisihuanxi Rd, Beijing, 100190, P. R. China. [∥]Present address: University of California, Berkeley, Department of Chemical and Biomolecular Engineering Berkeley, CA 94720-1462.

ABSTRACT We present a method for forming ordered rhodium nanostructures on a solid support. The approach makes use of a block copolymer to create and assemble rhodium chloride nanoparticles from solution onto a surface; subsequent plasma and thermal processing are employed to remove the polymer and fully convert the nanostructures to metallic rhodium. Films cast from a solution of the triblock copolymer poly(styrene-*b*-2-vinyl pyridine-*b*-ethylene oxide) dissolved in toluene with rhodium(III) chloride hydrate were capable of producing a monolayer of rhodium nanoparticles of uniform size and interparticle spacing. The nanostructures were characterized by scanning electron microscopy, X-ray photoelectron spectroscopy, and atomic force microscopy. The electrocatalytic performance of the nanoparticles was investigated with AC impedance spectroscopy. We observed that the addition of the particles to a model solid oxide fuel cell anode provided up to a 14-fold improvement in the anode activity as evidenced by a decrease in the AC impedance resistance. Examination of the anode after electrochemical measurement revealed that the basic morphology and distribution of the particles were preserved.

A grand challenge for solid oxide fuel cells (SOFCs) is to become cost-competitive with entrenched methods of large-scale, stationary power generation, *e.g.*, coal-fired power. In contrast to combustion, SOFCs can provide electrical power with zero carbon emissions and the highest known fuel-to-power conversion efficiencies.[1] However, by the metric of cost per watt, SOFCs are nearly a factor of 10 more expensive. Improved performance could change this, and although efficiencies of working devices are high, it is believed that significant gains in overall performance are possible with combined advances in key device components.[2,3]

One area of potential improvement is the anode. An SOFC is an electrochemical device comprised of a solid oxide electrolyte placed between an anode and a cathode. At the anode, the fuel, *e.g.*, hydrogen, is electrochemically oxidized by oxide ions arriving from the electrolyte, and the resulting flow of electrons (current) is sent to an external circuit. A conventional anode is a porous composite formed of metal, typically Ni, and the ceramic electrolyte, typically yttria-stabilized zirconia, components with percolating ionic, electronic and gas transport pathways. The performance of such a cermet (ceramic-metal) anode is, in large part, determined by its electrocatalytic activity, motivating designs that attempt to maximize the number of the gas-metal-ceramic contact points, as these triple-phase-boundaries (TPBs) serve as the reaction sites, while maintaining favorable transport characteristics.[4−6]

Several studies have indicated it is possible to increase electrochemical activity of cermet SOFC anodes through the introduction of metal nanoparticles. Zhu *et al.* demonstrated that a composite anode with Ni nanoparticles dispersed by impregnation has a power density more than double its untreated counterpart.[7] Kobsiriphat *et al.* showed that Ni and Ru nanoparticles

introduced by way of thermally driven diffusion and clustering also enhance power density.[8] Similarly, Gross *et al.* observed a sharp increase in anode activity upon impregnation of Pd, Ni and even Cu nanoparticles into SOFC anodes.[9] Whereas Kim *et al.* have shown the particular utility of palladium-ceria core–shell nanoparticles for such applications.[10] These results demonstrate the potential benefits of metal nanoparticles in SOFCs, and they motivate efforts to develop fabrication methods for the precise control of nanoparticle size and number density for ultimate maximization of fuel cell power output.

Block copolymer lithography (BCPL) has emerged as a versatile, solution-based technique for engineering nanoscale structures. Applied to the formation of nanoparticles on a surface (*aka* reverse micelle encapsulation), it can provide a high degree of control over particle size and interparticle spacing, *e.g.*, quasi-ordered arrays of uniformly sized nanoparticles.[11] Control is based on the choice of polymer, metal salt loading, and processing conditions.[12] Particle sizes can be as small as a few nanometers; for example, Kumar and Zhou produced arrays of (3.1 ± 0.5) nm Au nanoparticles with an interparticle spacing of (28.3 ± 3.7) nm.[13] Additionally, processing costs of BCPL are considerably lower than alternative methods offering similar levels of control, *e.g.*, electron beam lithography. Finally, BCPL is applicable to large areas, and it is not limited to planar surfaces, allowing rough surfaces and even powders to be coated.[14] Together, these features make BCPL a promising route for incorporating nanoparticles into SOFC anodes.

In principle, virtually any metal of interest as a catalyst, including those relevant to SOFCs, can be produced by BCPL to generate monodisperse, uniformly distributed nanoparticles.[15−17] Bimetallic particles are also possible.[18] The present study employs Rh as an example of the effectiveness of the BCPL approach. Rhodium-based catalysts have a number of important applications including controlling automobile exhaust emissions and reforming fuels such as biogas and diesel.[19,20] The high activity, thermal stability and resistance to carbon deposition of Rh render it particularly effective in SOFC anodes.[1] Even at ambient temperatures, Rh nanoparticles have shown promising electrocatalytic activity for formic acid oxidation.[21] Despite the flexibility of the BCPL approach and the importance of Rh as a catalyst, there is limited work on BCPL of rhodium.[22]

In this study, we present a robust method for synthesizing arrays of rhodium nanoparticles by BCPL. The particles were applied to a model SOFC anode, and the electrochemical activity for hydrogen oxidation was compared to that of an identical one without Rh nanoparticles. The model anode configuration consists of Pt current collectors applied to an oxide ion electrolyte and embedded beneath dense, mixed-conducting ceria. In contrast to conventional cermet anodes, the
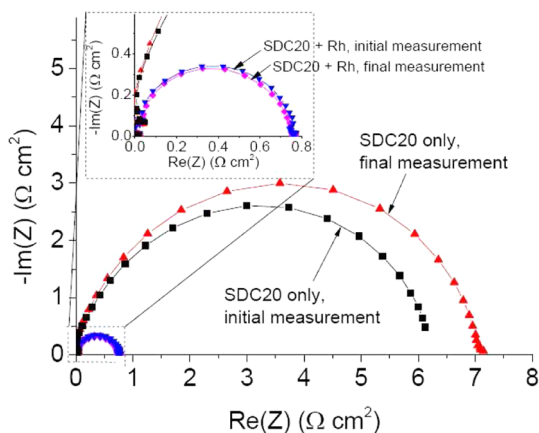

Figure 1. The low-frequency electrochemical reaction impedance response of SDC thin film cells measured at 650 °C, 5% H_2 with and without Rh nanoparticles as extracted from the measured full spectra (Figure SI-5 normalized by electrode area for each electrode. (∼2.5% H_2O, balance Ar). The 'final' measurements are data sets collected 40 min after the initial measurements. Changes in electrochemical activity for the Rh decorated anode are negligible.

electrochemical oxidation of hydrogen occurs on the surface of the exposed oxide, permitting a direct and quantitative assessment of the role of the Rh nanoparticles in the electrocatalysis.[23] Advantages of the BCPL synthesis technique and future directions are discussed.

RESULTS/DISCUSSION

Shown in Figure 1 are example impedance spectra collected at 650 °C under 5% H_2, ∼2.5% H_2O and balance Ar (total pressure of 1 atm), for anodes with and without Rh. For ease of comparison, only the impedance contribution of the electrochemical reaction is shown, and the response is normalized with respect to the area of the ceria electrode, irrespective of the presence of Rh particles (Figure SI-5). Most striking from these data is the significant decrease in the electrode impedance, represented by the diameters of the arcs in the spectra, upon application of the Rh. For this particular set of conditions, the difference amounts to a factor of 8; in some cases, the difference was as much as a factor of 14 (Table SI-1, Figure SI-6). The dramatic influence of Rh, on the one hand, confirms that the rate limiting step is the hydrogen electro-oxidation at the exposed anode surface (rather than electron transport through the mixed conducting ceria), and, on the other, demonstrates the exceptional activity of nanoparticulate Rh for enhancing this reaction rate.

Given the unconventional electrochemical reaction pathway in ceria-based anodes (reaction sites are not limited to triple-phase boundaries[23,24]), it is unclear whether triple-phase boundary density is a valuable metric in describing anodes incorporating ceria. In light of the predominant role of TPBs in standard SOFC anodes, however, it is of value to compare the TPB density generated in the present configuration to that of commercial cells.

Using the measured values for the particle density and particle diameters, we find the TBP areal density after heat treatment in hydrogen (but prior to electrochemical evaluation) to be $(9.2 \pm 2.0) \times 10^3$ m/cm^2, Figure 2. A recent study reports a typical cermet anode to be fabricated with a volumetric density of triple phase boundaries of 4.3×10^6 m/cm^{3}.[25] We convert from this volumetric value to an areal value by noting that the volume specific surface area of yttria stabilized zirconia (YSZ) in the same study is reported as $3.0 \ \mu m^{-1}$. Together, these imply an areal TPB density within the cermet anode of $\sim 1.4 \times 10^2$ m/cm^2, almost 2 orders of magnitude lower than what has been achieved here by the BPCL technique.

A typical concern with the use of nanoparticles at high temperatures is the potential for coarsening (*i.e.*, coalescence of particles) and hence loss of nanoscale features, particularly when exposed to electrochemical perturbation. To assess the extent to which such coarsening may occur, the Rh nanoparticles were imaged, by atomic force microscopy (AFM) techniques, both after exposure to high-temperature reducing conditions and additional exposure to electrochemical perturbation, Figure 2, panels a and b, respectively. We find that the basic particle morphology is preserved in both cases. In particular, the morphology of the thermally treated particles on YSZ, Figure 2a, is almost identical to that of the as-synthesized particles on Si, Figure 3a; the values of particle height and diameter are within statistical error of one another (specifically, the heights are (6.0 ± 1.8) and (5.5 ± 1.7) nm, respectively, whereas the particle diameters are (23 ± 5) and (21 ± 6) nm, respectively). The additional high temperature exposure and electrical perturbation induces slight, but non-negligible morphological changes. The particle height decreases slightly to (5.4 ± 1.2) nm and the diameter increases to (33 ± 5) nm. Relative to heat treatment alone, these values imply a doubling of the average particle projected area and an increase in the volume per particle by a factor of 1.8. Furthermore, the particle areal density decreases by a factor of 2.6 from $(1.28 \pm 0.05) \times 10^{11}$ to $(5.0 \pm 0.8) \times 10^{10}$ particles/cm^2. Geometrically this is approximately equivalent to the dimensional changes that would result from the merging of two particles into one during the electrochemical evaluation. Mechanistically, however, Ostwald ripening, in which large particles grow at the expense of smaller ones, is considered more likely based on the observed changes in particle size distribution, Figure SI-3. In terms of TPB density, the morphological changes correspond to a decrease from the initial (postheat treatment) value of $(9.2 \pm 2.0) \times 10^3$ to $(5.2 \pm 1.1) \times 10^3$ m/cm^2. That the extent of coarsening is rather limited may be the result of the high melt temperature of Rh (1966 °C); remarkable thermal stability has been reported previously for this metal.[26]
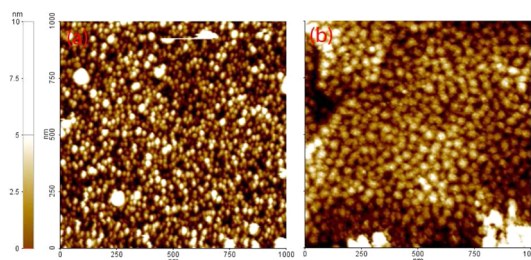

Figure 2. AFM images of Rh nanoparticles on a thin film of SDC on YSZ (a) after annealing under flowing hydrogen for 2 h at 600 °C and (b) after annealing in 0.1% H$_2$, 2.5% H$_2$O, balance Ar at 650 °C and subsequent exposure to electrochemical measurement conditions amounting to a total time of 24 h at temperatures of 500−650 °C under a range of reducing conditions (SI-E).
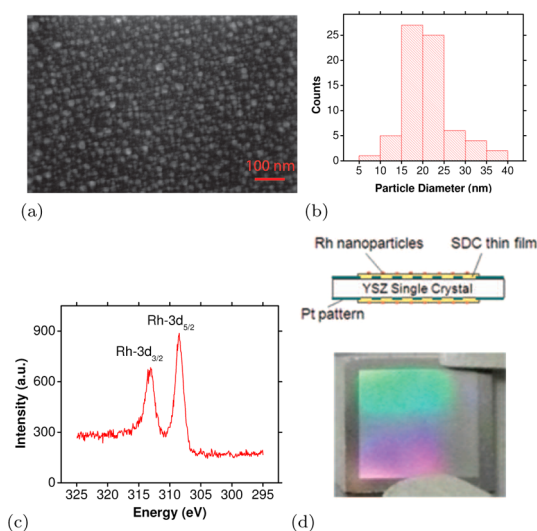

Figure 3. (a) SEM image of Rh nanoparticles cast on a Si support by BCPL with the triblock copolymer poly(styrene-*b*-2-vinyl pyridine-*b*-ethylene oxide) dissolved in toluene. (b) Histogram of particle diameters. The average diameter is (21 ± 6) nm. The average interparticle spacing is (6 ± 4) nm. (c) XPS spectrum of Rh nanoparticles on Si after annealing in hydrogen at 650 °C. (d) (top) Schematic of the symmetric cell used to measure the electrocatalytic activity of the Rh nanoparticles (side view). (The thickness of the layers is not in proportion to the actual physical dimensions.) The thickness of the YSZ layer is 0.5 mm and the thickness of each of the SDC films is about 1 μm. (d) (bottom) Image of the symmetric cell anode. The external dimensions of the cell are (1×1) cm, and the SDC thin film region (the bright square in the middle), which is over the Pt pattern, is (8×8) mm.

An immediate question that arises is that of the role of such morphological changes on electrochemical activity. Overall, we did observe an increase in the electrode impedance over the course of the electrochemical characterization experiments. However, the contribution of particle coarsening to this behavior is unknown. It has been observed that thin-film ceria based anodes degrade when examined under conditions of high relative humidity, most likely due to induced Si segregation to the surface.[27] In the present study, the electrodes with and without Rh generally degraded at the same rate, with the exception of

greatly diminished degradation rates for the Rh nanoparticle decorated sample at conditions of high temperature (650 °C) and low hydrogen partial pressure (5 and 20% H_2). Thus, Rh nanoparticle coarsening over the time scale observed here plays at most a minor role in inducing changes in electrochemical behavior. Rh can diminish degradation rates under some conditions, and, ultimately, the Rh-decorated electrodes retain, under all conditions, much higher activities than those without Rh, irrespective of degradation behavior. In sum, while changes in impedance response over time have complicated the analysis of the role of Rh in enhancing electrochemical activity, it is apparent that nanoparticles of this metal are tremendously beneficial for improving fuel cell performance.

CONCLUSION

From this work, we can conclude that the method described here is capable of forming metallic Rh nanoparticles that are (1) well ordered, (2) of uniform size, (3) robust, and (4) electrochemically active. The synthesis is scalable and inexpensive, making it attractive for applications in which fabrication cost is a driving consideration. Rhodium is normally employed as a reforming catalyst in SOFCs, and here, we show that it can, when deposited on mixed-conducting doped ceria, be used as a high temperature electrocatalyst as well. The uniformity in size and spacing of the particles provided by the BCPL method allowed us to measure the TPB density and observe the slight changes that occurred through the course of electrochemical evaluation. The presence of the particles improved the overall anode performance indicating that, in our model geometry, electrocatalysis is not limited by transport of either ions or electrons through the dense SDC layer, but rather by the reaction at the SDC/gas interface. While initial studies indicate minimal changes to particle morphology, further work will be needed to verify the long-term stability of such particles under SOFC operating conditions. The BCPL method presented allows a precise means for applying a costly material to a surface, and this is useful for both studying the effect of particle size and spacing as well as minimizing costs for commercial applications. A feature of forming the nanostructures by the BCPL method is that the particles have intimate and well-defined attachment to the surface,[16] and for SOFCs and other electrochemical or catalytic devices, this allows the triple phase boundaries to be controlled with the choice of polymer and processing conditions. Because BCPL is not limited to planar surfaces, it has the potential to be incorporated with traditional cermet-based anode designs. These are subjects for future studies.

METHODS

The nanoparticle arrays were prepared in the following manner: 24.9 mg of the triblock copolymer poly(styrene-*b*-2-vinyl pyridine-*b*-ethylene oxide, (PS(32000-P2VP(1300)-EO-(3000))) (P4866-S2VPEO, Polymer Source, Inc.) was dissolved in 5 mL of toluene (Omnisolv, EMD Chemicals). The solution was stirred vigorously for several days before adding 11.1 mg of rhodium(III) chloride hydrate (450286, Sigma-Aldrich) in a dry environment. Stirring was continued for several more days. The solution was spun-cast onto the sample substrates at 2000 rpm for 60 s and allowed to dry in room air. The sample was then placed in an oxygen plasma (Technics PlanarEtch II model 750) for 25 min at 85 W and 250 mTorr to remove the polymer. The samples were removed from the plasma cleaner and then baked at 650 °C under flowing hydrogen for 5 h. Other copolymers and solvents were explored, and these results are presented in the Supporting Information (SI-A).

The morphology and the interparticle spacing were examined by scanning electron microscopy (SEM) and AFM. An SEM image of the particles cast on a mechanical-grade silicon wafer is shown in Figure 3a. Image analysis reveals the average particle diameter to be (21 ± 6) nm, and the particle size distribution is shown in Figure 3b. The interparticle spacing was determined to be (6 ± 4) nm, implying ~55% coverage of the surface by Rh. The limit of the spatial resolution between particles was found to be about 2 nm. The average rhodium particle height on silicon is (5.5 ± 1.7) nm as measured by AFM (noncontact mode) (Figure SI-2). The differences in the average particle heights h and diameters d, i.e., $d > h$, indicate that the general shape of the particles is hemispherical cap rather than a full sphere.[16]

X-ray photoelectron spectroscopy (XPS) was used to verify the metallic state of the rhodium nanoparticles. The XPS binding energy spectrum of a monolayer of the particles on Si is shown in Figure 3c. The Rh-3$d_{5/2}$ and Rh-3$d_{3/2}$ binding energy peaks are present at 308.5 and 313.1 eV, respectively. The observed binding energy for Rh-3$d_{5/2}$ is higher than that of *bulk* rhodium, 307.2 eV. However, for nanoparticles the Rh-3$d_{5/2}$ value has been observed to vary from 307.0 to 308.5 eV depending on the substrate.[28] Additionally, the measured spin−orbit coupling of 4.6 eV is consistent with metallic rhodium, and it has been reported that in Rh thin films this value would increase if an oxide were present.[29] These XPS results indicate that the nanoparticles are metallic rhodium and would be expected to remain so during use in a fuel cell anode.

The model SOFC anode configuration used for the evaluation of Rh nanoparticle electrochemical activity consists of micropatterned Pt current collectors on either side of single crystal YSZ, overlain with a dense, thin layer of samaria-doped ceria (SDC), Figure 3d.[23] The SDC films are SDC20 (20 % samarium doped cerium oxide, $Sm_{0.20}Ce_{0.80}O_{1.90-\delta}$). The electrochemical oxidation of hydrogen occurs at the exposed ceria surface, and the significant electronic conductivity of SDC under reducing atmosphere in combination with the thinness of the SDC film (1 μm) allows electrons to migrate from the reaction sites to the embedded Pt current collector without measurably adding to the overall cell resistance.[23,24,30] The situation contrasts that of conventional SOFC anodes in which the catalytic sites must be in direct contact with the percolating metal phase.[31] Such symmetric cells were evaluated with and without Rh nanoparticles. The characteristics of the Rh nanoparticles (size, size distribution, spacing) on the ridged SDC substrate (ridged due to the presence of the underlying Pt) were found to be similar to those on smooth Si. AC impedance spectra (10 mHz to 10 MHz) were collected using a four-probe configuration over a range of temperatures and reducing gas atmospheres (SI-E).

Supporting Information Available: Details of the preparation of block copolymer solutions, of the sample characterizations, and of the impedance measurements. This material is available free of charge *via* the Internet at http://pubs.acs.org.

REFERENCES AND NOTES

1. Singhal, S. C.; Kendall, K. Introduction to SOFCs. In *High Temperature and Solid Oxide Fuel Cells*; Singhal, S. C., Kendal, K., Eds.; Elsevier Science: Amsterdam, 2003; pp 1−22.

2. Zhu, H.; Kee, R. J. Thermodynamics of SOFC Efficiency and Fuel Utilization As Functions of Fuel Mixtures and Operating Conditions. *J. Power Sources* **2006**, *161*, 957–964.

3. Wachsman, E. D.; Lee, K. T. Lowering the Temperature of Solid Oxide Fuel Cells. *Science* **2011**, *334*, 935–939.

4. Ansar, A.; Soysal, D.; Schiller, G. Nanostructured Functional Layers for Solid Oxide Fuel Cells. *Int. J. Energy Res.* **2009**, *33*, 1191–1202.

5. Kobsiriphat, W.; Madsen, B. D.; Wang, Y.; Marks, L. D.; Barnett, S. A. $La_{0.8}Sr_{0.2}Cr_{1-x}Ru_xO_{3-\delta}$ -$Gd_{0.1}Ce_{0.9}O_{1.95}$ Solid Oxide Fuel Cell Anodes: Ru Precipitation and Electrochemical Performance. *Solid State Ionics* **2009**, *180*, 257–264.

6. Gorte, R. J.; Vohs, J. M. Novel SOFC Anodes for the Direct Electrochemical Oxidation of Hydrocarbons. *J. Catal.* **2003**, *216*, 477–486.

7. Zhu, X. B.; Lu, Z.; Wei, B.; Chen, K. F.; Liu, M. L.; Huang, X. Q.; Su, W. H. Ni/SDC Nanoparticles Modified $La_{0.75}Sr_{0.25}Cr_{0.5}Fe_{0.5}O_{3-\delta}$ As Anodes for Solid Oxide Fuel Cells. *Electrochem. Solid-State Lett.* **2009**, *12*, B161–B164.

8. Kobsiriphat, W.; Madsen, B. D.; Wang, Y.; Shah, M.; Marks, L. D.; Barnett, S. A. Nickel- and Ruthenium-Doped Lanthanum Chromite Anodes: Effects of Nanoscale Metal Precipitation on Solid Oxide Fuel Cell Performance. *J. Electrochem. Soc.* **2010**, *157*, B279–B284.

9. Gross, M. D.; Vohs, J. M.; Gorte, R. J. An Examination of SOFC Anode Functional Layers Based on Ceria In YSZ. *J. Electrochem. Soc.* **2007**, *154*, B694–B699.

10. Kim, J.-S.; Wieder, N. L.; Abraham, A. J.; Cargnello, M.; Fornasiero, P.; Gorte, R. J.; Vohs, J. M. Highly Active and Thermally Stable Core-Shell Catalysts for Solid Oxide Fuel Cells. *J. Electrochem. Soc.* **2011**, *158*, B596–B600.

11. Spatz, J. P.; Mössmer, S.; Hartmann, C.; Möller, M.; Herzog, T.; Krieger, M.; Boyen, H.-G.; Ziemann, P.; Kabius, B. Ordered Deposition of Inorganic Clusters from Micellar Block Copolymer Films. *Langmuir* **2000**, *16*, 407–415.

12. Bansmann, J.; Kielbassa, S.; Hoster, H.; Weigl, F.; Boyen, H. G.; Wiedwald, U.; Ziemann, P.; Behm, R. J. Controlling the Interparticle Spacing of Au-Salt Loaded Micelles and Au Nanoparticles on Flat Surfaces. *Langmuir* **2007**, *23*, 10150–10155.

13. Kumar, S.; Zou, S. Electrooxidation of CO on Uniform Arrays of Au Nanoparticles: Effects of Particle Size and Interparticle Spacing. *Langmuir* **2009**, *25*, 574–581.

14. Croy, J.; Mostafa, S.; Heinrich, H.; Cuenya, B. Size-Selected Pt Nanoparticles Synthesized *via* Micelle Encapsulation: Effect of Pretreatment and Oxidation State on the Activity for Methanol Decomposition and Oxidation. *Catal. Lett.* **2009**, *131*, 21–32.

15. Lu, J.; Yi, S. S.; Kopley, T.; Qian, C.; Liu, J.; Gulari, E. Fabrication of Ordered Catalytically Active Nanoparticles Derived from Block Copolymer Micelle Templates for Controllable Synthesis of Single-Walled Carbon Nanotubes. *J. Phys. Chem. B* **2006**, *110*, 6655–6660.

16. Behafarid, F.; Cuenya, B. R. Nanoepitaxy Using Micellar Nanoparticles. *Nano Lett.* **2011**, *11*, 5290–5296.

17. Glass, R.; Moller, M.; Spatz, J. Block Copolymer Micelle Nanolithography. *Nanotechnology* **2003**, *14*, 1153–1160.

18. Croy, J. R.; Mostafa, S.; Hickman, L.; Heinrich, H.; Cuenya, B. R. Bimetallic Pt-Metal Catalysts for the Decomposition of Methanol: Effect of Secondary Metal on the Oxidation State, Activity, and Selectivity of Pt. *Appl. Catal., A* **2008**, *350*, 207–216.

19. Murphy, D. M.; Richards, A. E.; Colclasure, A. M.; Rosensteel, W.; Sullivan, N. Biogas Fuel Reforming for Solid Oxide Fuel Cells. *ECS Trans.* **2011**, *35*, 2653–2667.

20. Karatzas, X. Ph.D. Thesis, KTH Royal Institute of Technology, 2011.

21. Sathe, B. R.; Balan, B. K.; Pillai, V. K. Enhanced Electrocatalytic Performance of Interconnected Rh Nano-Chains Towards Formic Acid Oxidation. *Energy Environ. Sci.* **2011**, *4*, 1029–1036.

22. Bronstein, L. M.; Chernyshov, D. M.; Timofeeva, G. I.; Dubrovina, L. V.; Valetsky, P. M.; Khokhlov, A. R. The Hybrids of Polystyrene-*block*-Poly(ethylene oxide) Micelles and Sodium Dodecyl Sulfate in Aqueous Solutions: Interaction with Rh Ions and Rh Nanoparticle Formation. *J. Colloid Interface Sci.* **2000**, *230*, 140–149.

23. Chueh, W. C.; Hao, Y.; Jung, W.; Haile, S. M. High Electrochemical Activity of the Oxide Phase in Model Ceria Pt and Ceria Ni Composite Anodes. *Nat. Mater.* **2012**, *11*, 155–161.

24. Lai, W.; Haile, S. M. Impedance Spectroscopy as a Tool for Chemical and Electrochemical Analysis of Mixed Conductors: A Case Study of Ceria. *J. Am. Ceram. Soc.* **2005**, *88*, 2979–2997.

25. Wilson, J. R.; Kobsiriphat, W.; Mendoza, R.; Chen, H. Y.; Hiller, J. M.; Miller, D. J.; Thornton, K.; Voorhees, P. W.; Adler, S. B.; Barnett, S. A. Three-Dimensional Reconstruction of a Solid-Oxide Fuel-Cell Anode. *Nat. Mater.* **2006**, *5*, 541–544.

26. Chueh, W. C.; Shao, Z. P.; Haile, S. M. Tunability of Propane Conversion over Alumina Supported Pt and Rh Catalysts. *Top. Catal.* **2007**, *46*, 402–413.

27. Chueh, W. C. Ph.D. Thesis, California Institute of Technology, 2010.

28. Zafeiratos, S.; Nehasil, V.; Ladas, S. X-ray Photoelectron Spectroscopy Study of Rhodium Particle Growth on Different Alumina Surfaces. *Surf. Sci.* **1999**, *433*, 612–616.

29. Marot, L.; Mathys, D.; Temmerman, G. D.; Oelhafen, P. Characterization of Sub-Stoichiometric Rhodium Oxide Deposited by Magnetron Sputtering. *Surf. Sci.* **2008**, *602*, 3375–3380.

30. Jung, W.; Dereux, J. O.; Chueh, W. C.; Hao, Y.; Haile, S. M. High Electrode Activity of Nanostructured, Columnar Ceria Films for Solid Oxide Fuel Cells. *Energy Environ. Sci.* **2012**, *5*, 8682–8689.

31. Atkinson, A.; Barnett, S.; Gorte, R. J.; Irvine, J.; McEvoy, A. J.; Mogensen, M.; Singhal, S. C.; Vohs, J. Advanced Anodes for High-Temperature Fuel Cells. *Nat. Mater.* **2004**, *3*, 17–27.